Journal of
Materials Chemistry C

PAPER

View Article Online
View Journal | View Issue

Cite this: J. Mater. Chem. C, 2016, 4, 9235

Conductive single nanowires formed and analysed on microfluidic devices†

Yanlong Xing,[ab] Norbert Esser[b] and Petra S. Dittrich*[c]

Received 4th July 2016,
Accepted 3rd September 2016

DOI: 10.1039/c6tc02791a

www.rsc.org/MaterialsC

In this work, we studied the formation of fibres and particles made of metal salts and derivatives of tetrathiafulvalene (TTF) on a microfluidic device and in a conventional reaction flask, and characterized their morphologies, optical properties and electrical conductivities. A series of uniform one-dimensional (1D) structures were successfully formed *via* charge transfer interactions at the interface of two laminar streams on the microdevice. In general, these structures were significantly thinner and longer than those obtained in the standard bulk approach. The reaction between metal ions and different TTF derivatives indicated that the high planarity and strong molecular interaction of TTF derivatives are beneficial for nanowire formation. The conductivities of these metal-tetrathiafulvalene (M-TTF) and metal-formyl-tetrathiafulvalene (M-FTTF) nanowires were in the range of 10^{-1} to 10^{1} S cm^{-1} at room temperature, being one to two orders of magnitude greater than those of metal-bis(ethylenedithio)tetrathiafulvalene (M-BEDT-TTF) (4.8×10^{-3} to 1.2×10^{-2} S cm^{-1} at room temperature). However, not all combinations of metal salts and TTF derivatives yielded fibres. In many cases, we obtained particles or dendritic structures both in bulk reactions and on the microdevice. Hence, our study provides a comprehensive overview of the morphologies of the products obtained from reactions of metal salts and TTF including different commercially available derivatives.

1 Introduction

Single nanowire devices are at the forefront of advanced nanoscience as they are key materials in nanoelectronics and nanosensors.[1–3] In the past few decades, increasing research interest has been focused on developing new 1D structures, with improved control over morphologies and size distribution. Different kinds of nanostructures were reported including conductive polymers, inorganic materials and metal–organic compounds.[4–7] Among the metal–organic substrates, tetrathiafulvalene (TTF) has been widely explored due to its tunable electronic and optical properties and the flexibility of the structures, and is of great interest for building nanodevices and nanosensors.[8–10]

TTF is known as an excellent electron donor and can react with transition metal ions to form charge transfer complexes.[11–13] In previous work, the charge transfer between transition metal ions (Cu(II), Fe(III), Ru(III), Rh(III) *etc.*) and TTF derivatives has been studied, as well as the conductivities of their powder products.[14–16] In addition, the formation of fibre structures formed from Au[17] and Pb[18] with TTF and its derivatives were reported. In TTF-based charge transfer complexes, the mixed-valence states of TTF composed of neutral molecules and cation radicals were proved.[15,19] The common feature in these structures was the stacking of the TTF units, with metal units coordinated to the sulphur atoms in the stacks.[14,19,20] The morphologies of these complexes were affected by metal ions, different TTF derivatives, as well as the experimental variables *e.g.* solvents.

For the above-mentioned TTF-based compounds, a systematic study is missing, in which the reaction products of the various combinations of metal precursors and TTF derivatives are thoroughly characterized. This detailed study of these parameters will be useful for developing advanced single nanowire devices. In addition, nano-/microwires derived from metal-TTF charge transfer compounds *e.g.* gold-tetrathiafulvalen (Au-TTF), have been proved to be sensing elements by fast electronic[21] or optical[22] readout. Thus, for further application purposes, it is of great importance to sort out the metal-TTF (and derivatives), which can easily form quasi-1D single wire structures under various experimental conditions.

In this work, we performed the microfluidic-guided synthesis of a series of TTF-based metal–organic structures by using variable transition metal ions and TTF derivatives in different solvents. The aim is to explore single nanowires with good

[a] School of Analytical Sciences Adlershof, Humboldt-Universität zu Berlin, Germany
[b] Leibniz-Institute for Analytical Sciences, ISAS, Berlin, Germany
[c] Department of Biosystems Science and Engineering, ETH Zürich, Switzerland. E-mail: petra.dittrich@bsse.ethz.ch

† Electronic supplementary information (ESI) available: Structures of TTF derivatives, SEM images, IR and Raman spectra, EA results, EDX-SEM spectra, optical images and conductivity results of M-TTF and derivatives. See DOI: 10.1039/c6tc02791a

conductivity behaviour for further developing advanced nanodevices. Generally, metal ions including Au(III), Cu(I), Cu(II), Fe(II), Fe(III), Co(II), Ni(II), Mn(II), Zn(II) and organic ligands, which have TTF redox-active moieties including TTF, 2-formyl TTF (FTTF), bis(ethylenedithio)tetrathiafulvalene (BEDT-TTF), tetrakis(ethylthio)tetrathiafulvalene (TET-TTF) and 2,3,6,7-tetrakis(2-cyanoethylthio)tetrathiafulvalene (TCE-TTF) were used. These reactions were performed on a microfluidic device,[6,23,24] where the precursors reacted at the interface of two laminar streams. The formed structures were characterized using scanning electron microscopy (SEM) and optical microscopy, and the obtained fibres were further analysed using UV-Vis absorption, infrared (IR) and Raman spectroscopy, elemental analysis (EA), energy dispersive X-ray spectroscopy (EDX) and conductivity measurements. In addition, the effect of the substitute groups of the TTF derivatives on wire formation and conductive properties was compared and discussed.

2 Experimental

2.1 Materials

Acetonitrile (CH_3CN, 99.8+%), cobalt(II) chloride hexahydrate ($CoCl_2{\cdot}6H_2O$, 98%), copper(I) chloride powder (CuCl, 97%), copper(II) chloride powder ($CuCl_2$, 99%), gold(III) chloride trihydrate ($HAuCl_4{*}3H_2O$, 99+% trace metal basis), iron(II) chloride tetrahydrate ($FeCl_2{\cdot}4H_2O$, $\geq$99%), iron(III) nitrate ($Fe(NO_3)_3{\cdot}4H_2O$, $\geq$98%), methanol (CH_3OH, 99.8+%), nickel(II) chloride hexahydrate ($NiCl_2{\cdot}6H_2O$, 99.9%) and tetrahydrofuran (THF, anhydrous, $\geq$99.9%) were all purchased from Sigma-Aldrich (Buchs, Switzerland). Iron(III) chloride anhydrous ($FeCl_3$, 98%), and manganese(II) chloride tetrahydrate ($MnCl_2{\cdot}4H_2O$, 99+%) were obtained from Acros Organics (Basel, Switzerland). Copper(II) nitrate trihydrate ($Cu(NO_3)_2{\cdot}3H_2O$, 98+%) and zinc chloride ($ZnCl_2$, >98%) were purchased from Fluka (Buchs, Switzerland). BEDT-TTF, FTTF (>98%, GC), TCE-TTF, TET-TTF and TTF (>98.0%, GC) were obtained from TCI (Eschborn, Germany). Cobalt(II) nitrate hexahydrate ($Co(NO_3)_2{\cdot}6H_2O$, $\geq$99.0%), and zinc nitrate hexahydrate ($Zn(NO_3)_2{\cdot}6H_2O$, extra pure) were purchased from MERCK (Merck Schuchardt OHG, Hohenbrunn, Germany). Nickel(II) nitrate hexahydrate ($Ni(NO_3)_2{\cdot}6H_2O$, GR for analysis) was purchased from VWR International AG (Dietikon, Switzerland).

2.2 Microchip design and fabrication

The microchip designs were based on our chip designs for the synthesis of Au-TTF wires and other coordination polymers.[6,24] Images are given in Fig. S1 (ESI†). The microreactors were prepared by soft lithography using polydimethylsiloxane (PDMS). The detailed fabrication procedure for the master mould, the microchip and the glass slides with the microelectrodes can be found elsewhere.[21,25] Generally, four-inlet microchips were used, where the inner channels were used for the precursor supply, and the outer channels for the supply of pure solvent. The additional solvent streams focused the inner streams, and were referred to as sheath flows. The widths of the inlet microchannels and the main channel were 100 and 300 μm, respectively. The heights of all the channels were 20 μm. The total length of the main reactor channel was 1 cm. In some experiments, two-inlet microchips were used. Here, the inlet channels were 150 μm wide and the main channel had a width of 300 μm, the height was again 20 μm.

2.3 Synthesis

The reagents were loaded into plastic syringes and supplied through tubing into the chip *via* a syringe pump system (neMESYS module, Cetoni GmbH Korbußen, Germany) that controlled individual flow rates for the microchannel. The reactions between transition metal salts with TTF and FTTF were performed on four-inlet microchips as the synthesis of Au-TTF. Generally, flow rates of 500, 50, 50, 500 ($\mu L\ min^{-1}$) were used for channel A, B, C and D (see Fig. 1a). The two reactants were supplied from channel B and C at 50 $\mu L\ min^{-1}$. Two side streams of solvents were supplied from channel A and D at 500 $\mu L\ min^{-1}$. Eluted solutions from the microchips were collected and diluted 5 times with solvent (final concentration, approx. 0.06 mM) for UV-Vis measurements. The eluted structures were collected, filtered, washed with pure solvents and dried under a vacuum for undergoing FT-IR spectroscopy. In addition, the eluted structures from the chips were dropped onto clean glass slides (Thermos Scientific, Menzel-Gläser, Nr. 3) and dried under nitrogen (N_2) gas. Then the glass slides with the structures were gently rinsed with di-ionized water for 30 s and dried under a slow stream of N_2 gas before undergoing Raman measurement, SEM imaging and EDX measurement. In the SEM and EDX experiments, the glass slides with the samples were sputtered with Au/Pd (9/1) first and then mounted onto a sample holder for measurement.

In some cases, the structures were generated on a two-inlet chip (Fig. S1, ESI†) and compared with those formed on the four-inlet chip. Here, only the metal salts and the TTF derivative solutions were supplied at a flow rate of 100 ($\mu L\ min^{-1}$) in each channel.

The following concentrations were used:

Synthesis of CuX_2-TTF (or FTTF) (X = Cl^-, NO_3^-) complexes. CuX_2 (X = Cl^-, NO_3^-) (6 mM in CH_3CN or CH_3OH) and TTF (24 mM in CH_3CN or CH_3OH) or FTTF (24 mM in CH_3CN).

Synthesis of FeX_3-TTF (or FTTF) (X = Cl^-, NO_3^-) complexes. FeX_3 (X = Cl^-, NO_3^-) (6 mM in CH_3CN or CH_3OH) and TTF (21 mM in CH_3CN or CH_3OH) or FTTF (21 mM in CH_3CN).

Synthesis of M-BEDT-TTF. $HAuCl_4$, CuX_2 (X = Cl^-, NO_3^-), FeX_3 (X = Cl^-, NO_3^-) (0.06 mM in CH_3OH) and BEDT-TTF (0.24 mM in THF).

Synthesis of M-TET-TTF and M-TCE-TTF. $HAuCl_4$ (1.5 mM), $CuCl_2$ (1.5 mM) and TET-TTF (6 mM), TCE-TTF (6 mM) were used on two-inlet microchips separately. All dissolved in CH_3CN.

2.4 Characterization

The UV-Vis spectra were recorded on a Genesys 10 UV Scanning spectrophotometer (190–1100 nm, Thermo Scientific) with disposable polystyrene (PS) semi-micro cuvettes (BRAND). IR spectra were performed on a FTIR Tensor 27 Infrared spectrophotometer (Bruker) equipped with a Bruker Golden Gate diamond ATR (Attenuated Total Reflection) cell. EA was performed by service of the Laboratory of Organic Chemistry (LOC) of ETH

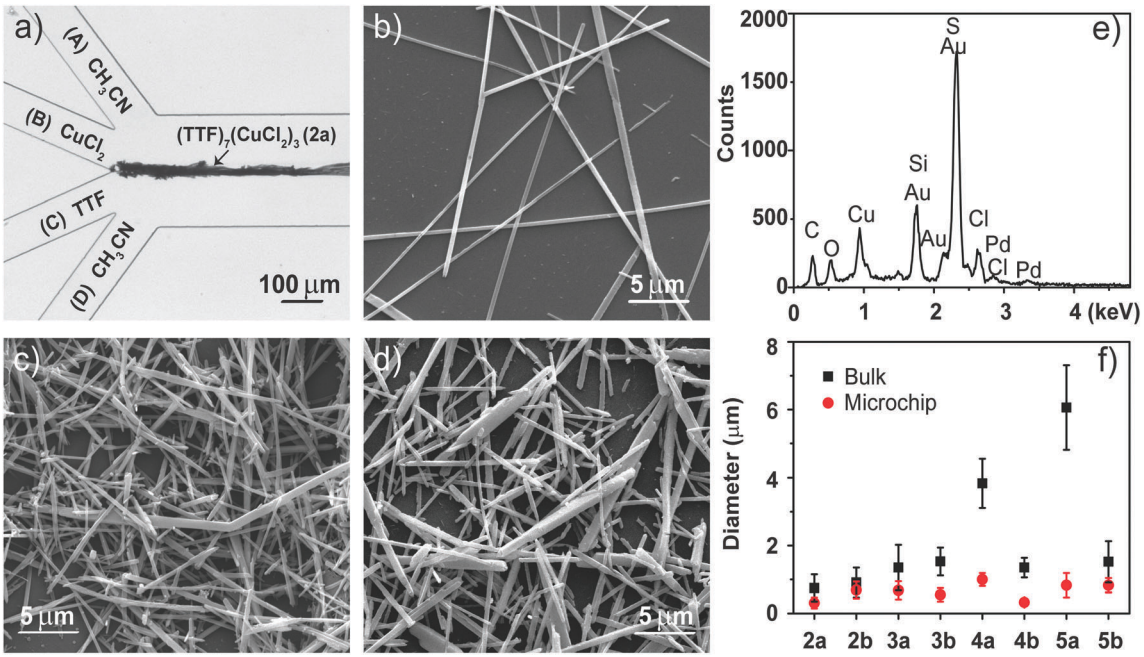

Fig. 1 Synthesis of wires, exemplary for $(TTF)_7(CuCl_2)_3$ (**2a**). (a) Optical micrograph of the four-inlet microchip. Wire bundles are formed at the interface of the $CuCl_2$ (channel B, flow rate 50 μL min^{-1}) and TTF solutions (channel C, flow rate 50 μL min^{-1}) in CH_3CN. The solvent was also used as sheath flow, supplied from channel A and D, at flow rates of 500 μL min^{-1}. (b) SEM image of the wire structures obtained on the four-inlet microchip. (c and d) SEM images of the wire structures obtained on the two-inlet chip (flow rates of 100 : 100 μL min^{-1}) and in bulk synthesis. (e) EDX-SEM spectrum of **2a**. (f) Comparison of the diameters (μm) of the wires obtained from different M-TTF complexes synthesized in bulk (solid black square) and on four-inlet microchips (solid red dot). The average diameter and standard deviation were obtained from ten different wires for each complex. For the compounds in the horizontal axis (**2a**, **2b**, **3a**, **3b**, **4a**, **4b**, **5a**, **5b**), refer to the numbers in Table 1 (column 2).

Zurich. Raman spectra were obtained on a confocal Raman microscope (CRM 200, WITec GmbH, Germany) equipped with a Nd:YAG laser (λ = 532 nm) and a 50× objective (NA 0.5). The laser power was 0.37 mW, and the accumulation time was 15 s (hardware accumulation: 4). The SEM images and the EDX-SEM were obtained using a FEI Quanta 200 FEG at the Scientific Center for Optical and Electron Microscopy (ScopeM) of ETH Zurich. Coloured and polarized images were recorded on a stereo-microscope (AZ-100M, Nikon) equipped with a digital camera (Digital sight DS-Fi1, Nikon). Other optical images were taken on an inverted microscope (IX71, Olympus) equipped with a digital camera (UK1117, ABS) and standard filters.

For conductivity measurement, single nano-/microwires were aligned on pre-fabricated microelectrodes with a home-built micromanipulator. The conductivities of the structures were obtained by performing four-point probe measurements (current source) on a Keithley 2612 A system source meter.

3 Results and discussion

In this work, we selected various transition metal salts for the reaction with TTF and its derivatives (Fig. S2, ESI†). An overview is given in Table 1, showing the metal salts, solvents we used for the reaction, and the results of the various analytical examinations. In the following, the major findings for the reaction of TTF with various metal salts, particularly Cu(II) and Fe(III) salts, are discussed. Finally, the results for the TTF derivatives are presented.

3.1 Formation and analysis of M-TTF structures

Synthesis and analysis using optical microscopy and SEM. Fig. 1a–e shows exemplarily the reaction of $CuCl_2$ and TTF that was performed on a microdevice by supplying the two reactant solutions through channels B and C both at flow rates of 50 μL min^{-1}. The solvent, here CH_3CN, was supplied through channels A and D. The solvent streams with a flow rate of 500 μL min^{-1} focused the inner streams to a narrow reaction zone.[24] The reaction to $(TTF)_7(CuCl_2)_3$ (**2a**) occurred immediately as can be seen by the black product in Fig. 1a. The structures were flushed out of the channel and observed using SEM (Fig. 1b). For comparison, we also used a two-inlet microchip, *i.e.* without sheath flows (Fig. 1c), and we performed the reaction in a standard glass flask (Fig. 1d). As can be seen from the SEM images, the reaction in the four-inlet microdevice yielded the longest fibres with a smaller diameter than those obtained by the other approaches. The four-inlet microfluidic chip is preferred in the following because it provides a defined interface between the two laminar flowing precursor streams and confines the reaction zone by use of the sheath flow (compare Fig. 1a and Fig. S1a, ESI†). The wires assemble in this reaction zone in the direction of the flow. Furthermore, this chip design has the benefits that the wires are flushed out immediately and do not block the channel. Once outside, they are immediately diluted and do not react further.

Table 1 An overview of the experimental parameters, morphologies, conductivities and characterizations of the metal-TTF (and derivatives) complexes

				Properties				
Metal salts	No.	Solvent	Compound formula	Diameter bulk reaction [μm]	Diameter μfluidic reaction [μm]	Conductivities, σ^a S cm^{-1}	Characterization of structures	Ref.
I. Tetrathiafulvalene (TTF)								
$HAuCl_4$[b]	**1**	CH_3CN	$(TTFCl_{0.78})Au_{0.12}$	0.41–4.43	0.2–2.0	0.021	SEM/EDX-SEM/UV-Vis/IR/EA (see reference)	19, 21, 31
$CuCl_2$	**2a**	CH_3CN	$(TTF)_7(CuCl_2)_3$	0.75 ± 0.39 (Fig. 1f-**2a**)	0.31 ± 0.15 (Fig. 1f-**2a**)	1.13 (Fig. S11a, ESI)	SEM (Fig. 1b–d)/EDX-SEM (Fig. 1e)/UV-Vis (Fig. S8a, ESI)/IR (Fig. S9, ESI)/Raman (Fig. S10, ESI)/EA (Table S1, ESI)	15, 16, 27
	2b	CH_3OH	$(TTF)_2CuCl_2$	0.91 ± 0.43 (Fig. 1f-**2b**)	0.69 ± 0.25 (Fig. 1f-**2b**)	0.34 (Fig. S11b, ESI)	SEM (Fig. S3a and b, ESI)/ EDX-SEM (Fig. S6a, ESI)/UV-Vis (Fig. S8b, ESI)/IR (Table S2, ESI)/ Raman (Fig. S10, ESI)/EA (Table S1, ESI)	15, 16, 27
$Cu(NO_3)_2$	**3a**	CH_3CN	$(TTF)_4Cu(NO_3)_2$	1.35 ± 0.67 (Fig. 1f-**3a**)	0.68 ± 0.27 (Fig. 1f-**3a**)	0.31 (Fig. S11c, ESI)	SEM (Fig. S3c and d, ESI)/ EDX-SEM (Fig. S6b, ESI)/UV-Vis (Fig. S8b, ESI)/IR (Fig. S9, ESI)/ Raman (Fig. S10, ESI)/EA (Table S1, ESI)	16, 27
	3b	CH_3OH	$(TTF)_4Cu(NO_3)_2$	1.53 ± 0.41 (Fig. 1f-**3b**)	0.55 ± 0.22 (Fig. 1f-**3b**)	0.15 (Fig. S11d, ESI)	SEM (Fig. S3e and f, ESI)/ EDX-SEM (Fig. S6c, ESI)/UV-Vis (Fig. S8b, ESI)/IR (Table S2, ESI)/ Raman (Fig. S10, ESI)/EA (Table S1, ESI)	16, 27
$FeCl_3$	**4a**	CH_3CN	$(TTF)_5FeCl_3$	3.82 ± 0.71 (Fig. 1f-**4a**)	0.93 ± 0.09 (Fig. 1f-**4a**)	0.11 (Fig. S11e, ESI)	SEM (Fig. S4a and b, ESI)/ EDX-SEM (Fig. S7a, ESI)/UV-Vis (Fig. S8c, ESI)/IR (Table S2, ESI)/ Raman (Fig. S10, ESI)/EA (Table S1, ESI)	This work
	4b	CH_3OH	$(TTF)_5FeCl_3$	1.35 ± 0.28 (Fig. 1f-**4b**)	0.32 ± 0.05 (Fig. 1f-**4b**)	0.40 (Fig. S11f, ESI)	SEM (Fig. S4c and d, ESI)/EDX-SEM (Fig. S7b, ESI)/UV-Vis (Fig. S8c, ESI)/IR (Table S2, ESI)/Raman (Fig. S10, ESI)/EA (Table S1)	14
$Fe(NO_3)_3$	**5a**	CH_3CN	$(TTF)_5Fe(NO_3)_3$	6.05 ± 1.25 (Fig. 1f-**5a**)	0.83 ± 0.36 (Fig. 1f-**5a**)	0.35 (Fig. S11g, ESI)	SEM (Fig. S4e and f, ESI)/ EDX-SEM (Fig. S7c, ESI)/UV-Vis (Fig. S8c, ESI)/IR (Table S2, ESI)/ Raman (Fig. S10, ESI)/EA (Table S1, ESI)	This work
	5b	CH_3OH	$(TTF)_5Fe(NO_3)_3$	1.51 ± 0.61 (Fig. 1f-**5b**)	0.82 ± 0.21 (Fig. 1f-**5b**)	0.53 (Fig. S11h, ESI)	SEM (Fig. S4g and h, ESI)/ EDX-SEM (Fig. S7d, ESI)/UV-Vis (Fig. S8c, ESI)/IR (Table S2, ESI)/ Raman (Fig. S10, ESI)/EA (Table S1, ESI)	This work
Cu(I)Cl	**6**	CH_3CN	—	—	No structure (Fig. S5a, ESI)	—	UV-Vis (Fig. S8e and f, ESI)	This work
$FeCl_2$	**7**	CH_3OH	—	Needles (Fig. S5b, ESI)	Needles (Fig. S5c, ESI)	—	UV-Vis (Fig. S8e and f, ESI)	This work
$CoCl_2$	**8**	CH_3CN	—	—	No structure (Fig. S5d, ESI)	—	UV-Vis (Fig. S8e and f, ESI)	This work
$Co(NO_3)_2$	**9**	CH_3CN	—	Flakes (Fig. S5e, ESI)	Particles (Fig. S5f, ESI)	—	UV-Vis (Fig. S8e and f, ESI)	This work
$MnCl_2$	**10**	CH_3OH	—	—	Particles (Fig. S5g, ESI)	—	UV-Vis (Fig. S8e and f, ESI)	This work
$NiCl_2$	**11**	CH_3OH	—	Particles (Fig. S5h, ESI)	Particles (Fig. S5i, ESI)	—	UV-Vis (Fig. S8e and f, ESI)	This work
$Ni(NO_3)_2$	**12**	CH_3CN	—	Particles (Fig. S5j, ESI)	Particles/needles (Fig. S5k, ESI)	—	UV-Vis (Fig. S8e and f, ESI)	This work
$ZnCl_2$	**13**	CH_3CN	—	Particles (Fig. S5l, ESI)	Particles (Fig. S5m, ESI)	—	UV-Vis (Fig. S8e and f, ESI)	This work
$Zn(NO_3)_2$	**14**	CH_3CN	—	Rods (Fig. S5n, ESI)	Needles (Fig. S5o, ESI)	—	UV-Vis (Fig. S8e and f, ESI)	This work
II. 2-Formyl-tetrathiafulvalene (FTTF)								
$HAuCl_4$	**15**	CH_3CN	$(FTTF)_3AuCl_3$	Dendrites (Fig. S13a, ESI)	0.26 ± 0.14 (Fig. 3b)	0.66 (Fig. S15a, ESI)	SEM (Fig. 3a and b)/EDX-SEM (Fig. S18a, ESI)/UV-Vis (Fig. S12a, ESI)/IR (Fig. S16, ESI)/Raman (Fig. S17, ESI)/EA (Table S3, ESI)	This work

Table 1 (*continued*)

Metal salts	No.	Solvent	Compound formula	Properties: Diameter bulk reaction [μm]	Properties: Diameter μfluidic reaction [μm]	Properties: Conductivities, σ^a S cm^{-1}	Characterization of structures	Ref.
$CuCl_2$	**16**	CH_3CN	$(FTTF)_2CuCl_2$	Dendrites (Fig. S13b, ESI)	0.20 ± 0.08 (Fig. 3e)	0.84 (Fig. S15b, ESI)	SEM (Fig. 3d and e)/EDX-SEM (Fig. S18b, ESI)/UV-Vis (Fig. S12a, ESI)/IR (Fig. S16, ESI)/Raman (Fig. S17, ESI)/EA (Table S3, ESI)	This work
$Cu(NO_3)_2$	**17**	CH_3CN	—	Clusters (Fig. S14a, ESI)	Particles (Fig. S14c, ESI)	—	UV-Vis (Fig. S12a, ESI)	This work
$Fe(NO_3)_3$	**18**	CH_3OH	—	Clusters (Fig. S14d, ESI)	Particles (Fig. S14f, ESI)	—	UV-Vis (Fig. S12b, ESI)	This work
$FeCl_3$	**19**	CH_3OH	—	Dendrites (Fig. S14g, ESI)	Dendrites (Fig. S14i, ESI)	—	UV-Vis (Fig. S12b, ESI)	This work
$FeCl_2$	**20**	CH_3OH	—	FTTF-dendritic crystals (Fig. S14j, ESI)	FTTF-dendritic crystals (Fig. S14k, ESI)	—	UV-Vis (Fig. S12c, ESI)	This work
$ZnCl_2$	**21**	CH_3CN	—	FTTF-dendritic crystals (Fig. S14l, ESI)	FTTF-dendritic crystals (Fig. S14m, ESI)	—	UV-Vis (Fig. S12c, ESI)	This work
$Zn(NO_3)_2$	**22**	CH_3CN	—	FTTF-dendritic crystals (Fig. S14n, ESI)	FTTF-dendritic crystals (Fig. S14o, ESI)	—	UV-Vis (Fig. S12c, ESI)	This work
III. Bis(ethylenedithio)tetrathiafulvalene (BEDT-TTF)[c]								
$HAuCl_4$	**23**	CH_3CN	—	1.73 ± 0.61 (Fig. S21a, ESI)	0.56 ± 0.12 (Fig. 4a)	6.3×10^{-3} (Fig. S23a, ESI)	SEM (Fig. 4a)/UV-Vis (Fig. S20a, ESI)/EDX-SEM (Fig. S24b, ESI)	17
$CuCl_2$	**24**	CH_3OH	—	1.79 ± 0.31 (Fig. S21b, ESI)	0.59 ± 0.14 (Fig. S22a, ESI)	NA (Fig. S22b, ESI)	SEM (Fig. S22a, ESI)/UV-Vis (Fig. S20b, ESI)	20, 33, 36
$Cu(NO_3)_2$	**25**	CH_3OH	—	3.16 ± 0.82 (Fig. S21c, ESI)	2.11 ± 0.53 (Fig. 4b)	4.8×10^{-3} (Fig. S23b, ESI)	SEM (Fig. 4b)/UV-Vis (Fig. S20b, ESI)/EDX-SEM (Fig. S24c, ESI)	This work
$FeCl_3$	**26**	CH_3OH	—	1.68 ± 0.95 (Fig. S21d, ESI)	0.50 ± 0.12 (Fig. S22c, ESI)	NA (Fig. S22d, ESI)	SEM (Fig. S22c, ESI)/UV-Vis (Fig. S20c, ESI)	This work
$Fe(NO_3)_3$	**27**	CH_3OH	—	1.29 ± 0.59 (Fig. S21e, ESI)	0.47 ± 0.11 (Fig. 4c)	1.2×10^{-2} (Fig. S23c, ESI)	SEM (Fig. 4c)/UV-Vis (Fig. S20c, ESI)/EDX-SEM (Fig. S24d, ESI)	This work
IV. Tetrakis(ethylthio)tetrathiafulvalene (TET-TTF)								
$HAuCl_4$	**28**	CH_3CN	—	Crystals (Fig. S19a, ESI)	—	—	—	This work
$CuCl_2$	**29**	CH_3CN	—	Crystals (Fig. S19b, ESI)	—	—	—	This work
V. 2,3,6,7-Tetrakis(2-cyanoethylthio)tetrathiafulvalene (TCE-TTF)								
$HAuCl_4$	**30**	CH_3CN	—	Crystals (Fig. S19c, ESI)	—	—	—	This work

[a] σ refers to the conductivities of the specific measured single nanowires (see figure insets of Fig. 2, 3c, f and 4d–f) at room temperature. [b] Bulk results from our experiment; diameters of wires formed by microfluidics depend on the method; approx. conductivity (wire formed by diffusion, ~2 μm) was calculated from our previous work (ref. 21). [c] For BEDT-TTF a two-solvent system was used, with metal salts in CH_3OH and BEDT-TTF in THF; NA means that the conductive properties are not available due to experimental limitation.

In addition, the morphologies of the structures obtained from the reaction of TTF with Cu(II) and Fe(III) salts were studied (**2b**, **3a**, **3b**, **4a**, **4b**, **5a**, **5b**), which showed clear differences between bulk synthesis and four-inlet microchips (Fig. 1f, SEM images in Fig. S3 and S4, ESI†). All the wires resulting from the four-inlet microchip are in the nanometer range and smaller than those from the bulk synthesis, confirming that microfluidic synthesis is an advanced tool to control the formation of nanostructures.

Next, we investigated the reaction between TTF and other metal salts including CuCl (**6**), $FeCl_2$ (**7**), $CoCl_2$ (**8**), $Co(NO_3)_2$ (**9**), $MnCl_2$ (**10**), $NiCl_2$ (**11**), $Ni(NO_3)_2$ (**12**), $ZnCl_2$ (**13**) and $Zn(NO_3)_2$ (**14**) using optical microscopy. Here, the products showed various morphologies, but not 1D nano-/microstructures (Fig. S5, ESI†).

EDX and elemental (CHN) analysis. The components of the nanowires obtained from the microchips were characterized using EDX spectroscopy and are shown in Fig. 1e for **2a**, which clearly indicate C, Cu, S, and Cl elements. The results for the other Cu(II) and Fe(III) salts are depicted in Fig. S6 and S7 (ESI†). The EA results of these compounds are summarized in Table S1 (ESI†), which confirmed the chemical composition of the nanostructures of **2a**, **2b**, **3a**, **3b**, **4a**, **4b**, **5a** and **5b** quantitatively.

UV-Vis spectroscopy. The eluted solution from the microchips after the reaction were diluted and directly applied for UV-Vis investigation. As indicated in Fig. S8a (ESI†), TTF had weak absorbance at 436 nm, while $CuCl_2$ only showed a negligible absorption signal. In comparison, the spectrum of the eluted solution of **2a** exhibited an intense band at 436 nm and a new absorption band at 580 nm, which indicated the existence of a TTF radical cation, due to the electron transfer from TTF to Cu^{2+}.[16,26] The absorption spectra of the other complexes (**2b**, **3a**, **3b**, **4a**, **4b**, **5a**, **5b**)

at 580 nm are summarized and also indicate the electron transfer between TTF and Cu(II) (Fig. S8b, ESI†), as well as that of TTF and Fe(III) (Fig. S8c, ESI†), all without any interference from metal ions (Fig. S8d, ESI†). The differences in absorption intensities clearly showed that Cu(II) was a more powerful oxidizing agent in CH_3CN than in CH_3OH (Fig. S8a and b, $A_{2a} > A_{3a} > A_{2b} > A_{3b}$, ESI†), while Fe(III) showed a higher oxidative ability in CH_3OH than in CH_3CN (Fig. S8c, $A_{5b} > A_{5a} > A_{4b} > A_{4a}$, ESI†), in accordance with reported work.[27,28] For the precursors of Cu(I), Fe(II), Co(II), Mn(II), Ni(II), and Zn(II) ions and the products after their reactions with TTF, only negligible absorptions were observed at 580 nm (Fig. S8e and f, ESI†). Consequently, we made a comparison of the spectra from the different oxidised states of the same metal. In contrast to the spectra of solutions resulting from Cu(II) and TTF (**2a**, **2b**, Fig. S8a and b, ESI†), the spectrum of Cu(I) and TTF didn't exhibit obvious absorbance (**6**, Fig. S8f, ESI†). Similar results were observed for the spectra of solutions from Fe(III) and TTF (**4a**, **4b**, Fig. S8c, ESI†), and that of Fe(II) and TTF (**7**, Fig. S8f, ESI†). Thus, we can draw the conclusion that only higher oxidised states of Cu(II) and Fe(III) could induce the electron transfer from TTF to the corresponding metal ions in the experimental conditions applied in our work.

IR spectroscopy. The IR spectra were obtained for the M-TTF complexes which formed wire structures. As shown in the spectrum of **2a** (Fig. S9, ESI†), typical assignments at 1242 cm^{-1} (ν_{23}, CCH bend), 1082 cm^{-1} (ν_{15}, CCH bend), 814 cm^{-1} (ν_{16}, CS stretch), 804 cm^{-1} (ν_{25}, SCC bend), and 740 cm^{-1} (ν_{17}, CS stretch) were all between the IR assignments for the TTF^0 molecules and the TTF^+ cation, which indicates the mixed-valence state of this TTF-based material in the neutral and cation radical states.[15,29] Similar TTF bands were also observed for **3a** at 1245 cm^{-1} (ν_{23}, CCH bend), 817 cm^{-1} (ν_{16}, CS stretch) and 733 cm^{-1} (ν_{17}, CS stretch) (Fig. S9, ESI†). Specifically, the observed peak at 1312 cm^{-1} indicates the existence of nitrate[27,30] which formed anion columns in the resulting structures. In addition, the mixed-valence state of neutral and TTF cations in other TTF-based complexes (**2b**, **3a**, **3b**, **4a**, **4b**, **5a**, **5b**) were also confirmed by their IR spectra assignments (Table S2, ESI†). Thus, similar structures were formed for these M-TTF wires, with a backbone scaffold of TTF neutral and cation radicals stabilized with counter ions forming the 1D nanowires. To further prove the TTF components in the nanostructures, confocal Raman measurement were performed, in which the typical Raman peaks at around 500 cm^{-1} and 1420 cm^{-1} (Fig. S10, ESI†) were observed, similar to the spectra of Au-TTF (**1**) in our previous work.[22,31] The difference between **1** and **2b**, **3a**, **3b**, **4a**, **4b**, **5a**, and **5b** is that in the former structure, Au(III) ions were reduced to Au(0),[19] while in the latter structures, metal ions existed as low oxidised Cu(I) and Fe(II) when excess TTF was used.[14,15] The common features of the structures of these donor–acceptor complexes are, firstly the mix-valence state of the TTF stacking, and secondly the coordination of metal (Au(0))[19] and metal ion (Cu(I) and Fe(II)) to the sulphur atoms in the TTF stacks.[14]

Electrical properties. It was reported that partially charged TTF salts exhibited higher electrical conductivities than simple salts at room temperature.[29] Thus, we applied the nanowires obtained from M-TTF for conductivity investigation using a four-point probe measurement by aligning a single nanowire on pre-fabricated microelectrodes. The *I–V* curves of these complexes were obtained by measuring the source–drain voltage while sweeping the applied source–drain current at room temperature. As shown in Fig. 2, the *I–V* curves for **2b**, **3a**, **3b**, **4a**, **4b**, **5a** and **5b** are non-linear, which we assume is an indication of the

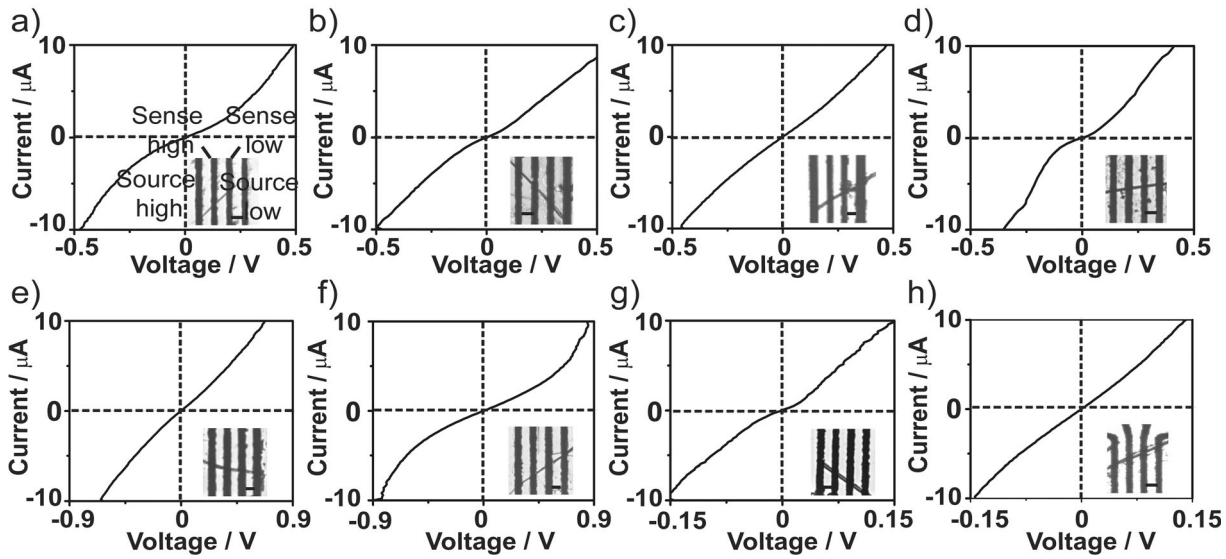

Fig. 2 Representative *I–V* curves of single nanowires of the M-TTF complexes obtained by four-point measurement. The two outer microelectrodes represent source high and source low, while the two inner electrodes represent sense high and sense low. (a) $(TTF)_7(CuCl_2)_3$ in CH_3CN (**2a**); (b) $(TTF)_2CuCl_2$ in CH_3OH (**2b**); $(TTF)_4Cu(NO_3)_2$ in (c) CH_3CN (**3a**) and in (d) CH_3OH (**3b**); $(TTF)_5FeCl_3$ in (e) CH_3CN (**4a**) and in (f) CH_3OH (**4b**); $(TTF)_5Fe(NO_3)_3$ in (g) CH_3CN (**5a**) and in (h) CH_3OH (**5b**). Figure insets show the alignment of single nanowires on the four microelectrodes, all the electrodes are connected to the source meter. The gaps between electrodes (scale bars) are 5 μm.

non-perfect contact, as the nanowires were simply aligned on the microelectrodes, without topside metallization performance. Similar conductive behaviour for **1** was observed in our previous work.[21] Different voltage ranges were shown for different nanowires with various diameters and lengths when the same current was applied. Thus, we made a comparison of the linear conductance of all the *I–V* curves in Fig. 2. The results indicated that all the nanowires exhibited high electrical conductivities from 10^{-1} to 10^{1} S cm^{-1} (Fig. S11, ESI†) at room temperature. In particular, **2a** showed the highest conductivity (σ = 1.13 S cm^{-1}), followed by **5b** (σ = 0.53 S cm^{-1}) and **4b** (σ = 0.40 S cm^{-1}).

Thus, with our proposed characterization technique, it is possible to measure the conductivities of single nanowires, for which the non-linear curves are caused by contact effects between the wire and microelectrodes, while the linear parts of the *I–V* curves show typical ohmic behaviour (Fig. S11, ESI†). In addition, the electron transfer of TTF to metal ions and the conductive behaviour of the induced fibres are influenced by the solvent used in the system.

3.2 Derivatives of TTF

Furthers studies on the reaction between transition metal salts and commercially available TTF derivatives were conducted. Firstly, FTTF, with an aldehyde functional group at the C_1 substitution of the TTF unit was further explored. The reactions of FTTF with $HAuCl_4$, Cu(II) and Zn(II) salts were performed in CH_3CN, while the reaction with Fe(III) salts was performed in CH_3OH. In the UV-Vis spectra of M-FTTF (Fig. S12, ESI†), the spectra of compounds **15**, **16**, **17**, **18** and **19** all exhibited side peaks at 580 nm, showing indications of charge transfer between these metal ions and FTTF. Various morphologies were observed for the products of M-FTTF from bulk synthesis and microchips. The reaction with $HAuCl_4$ and $CuCl_2$ yielded large dendrites in bulk synthesis (Fig. S13, ESI†), however, 1D wire structures were obtained on microchips (**15**, Fig. 3a and b; **16**, Fig. 3d and e). Although $Fe(NO_3)_3$ and $FeCl_3$ also induced the charge transfer with FTTF (UV-Vis spectra, Fig. S12b, ESI†), only dendrites and particles (**18**, Fig. S14d–f, ESI†) (**19**, Fig. S14g–i, ESI†), but not 1D wire structures were observed. For the other metal salts, only particles or dendrites were formed after reaction with FTTF, including $Cu(NO_3)_2$-FTTF (**17**), $FeCl_2$-FTTF (**20**), $ZnCl_2$-FTTF (**21**) and $Zn(NO_3)_2$-FTTF (**22**) (Fig. S14, ESI†).

In addition, *I–V* curves were measured using single aligned nanowires of Au-FTTF (**15**) and Cu-FTTF (**16**), which showed quasi-linear metallic behaviour properties (Fig. 3c and f). The electrical conductivities of measured **15** and **16** nanowires were calculated to be 0.66 S cm^{-1} and 0.84 S cm^{-1} (Fig. S15, ESI†), showing the conductive performance of M-FTTF nanowires at room temperature. The IR spectra of **15** and **16** indicated the mixed-valence state of FTTF stacks in these complexes (Fig. S16, ESI†). Interestingly, comparison of the IR assignments of compounds **15**, **16** with FTTF revealed that the aldehyde group (C═O) at around 1640 cm^{-1} remained after the formation of 1D structures, which made it possible for further modification on the wire by using aldehyde-active compounds. Furthermore, the Raman spectra (Fig. S17, ESI†) and EDX-SEM spectra (Fig. S18, ESI†) of **15** and **16** complexes, together with the EA results (Table S3, ESI†) demonstrated the components of metal chloride and FTTF in these structures both qualitatively

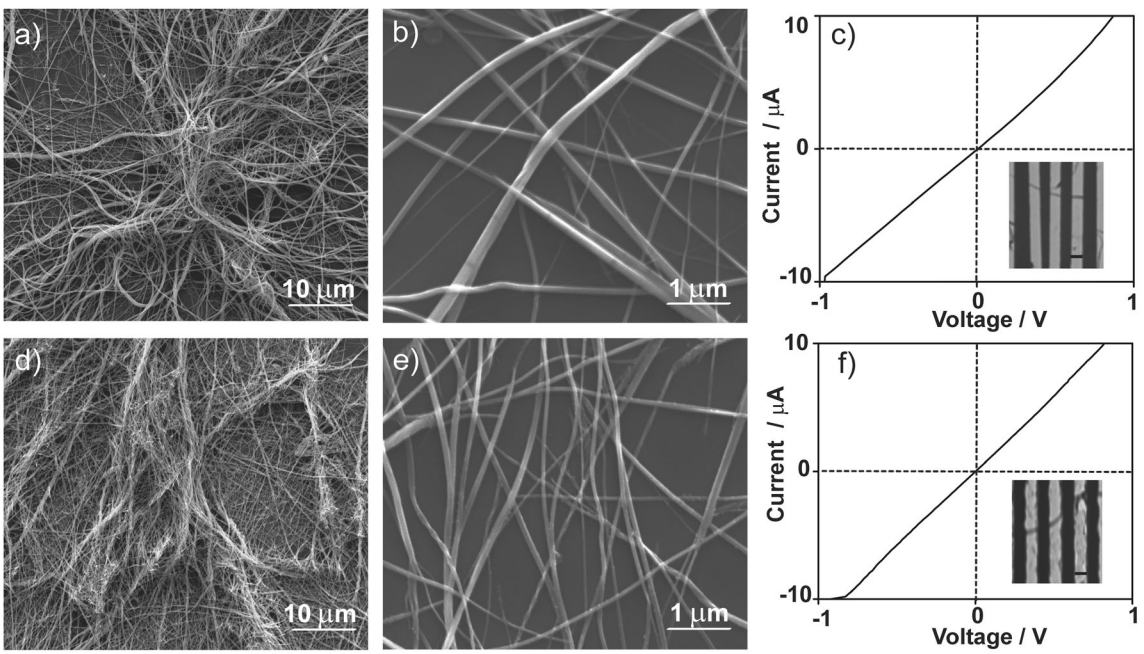

Fig. 3 SEM images of Au-FTTF (**15**) generated on (a) the two-inlet microchip (diameter, 0.39 ± 0.11 μm) and (b) the four-inlet microchip (average diameter, 0.26 ± 0.14 μm); (c) *I–V* curve of a single nanowire of **15** from the four-inlet microchip. SEM images of Cu-FTTF (**16**) generated on (d) the two-inlet microchip (diameter, 0.27 ± 0.13 μm) and (e) the four-inlet microchip (0.20 ± 0.08 μm); (f) *I–V* curve of a single nanowire of **16** formed on the four-inlet microchip. Figure insets in (c) and (f) show the aligned single nanowire on the microelectrodes.

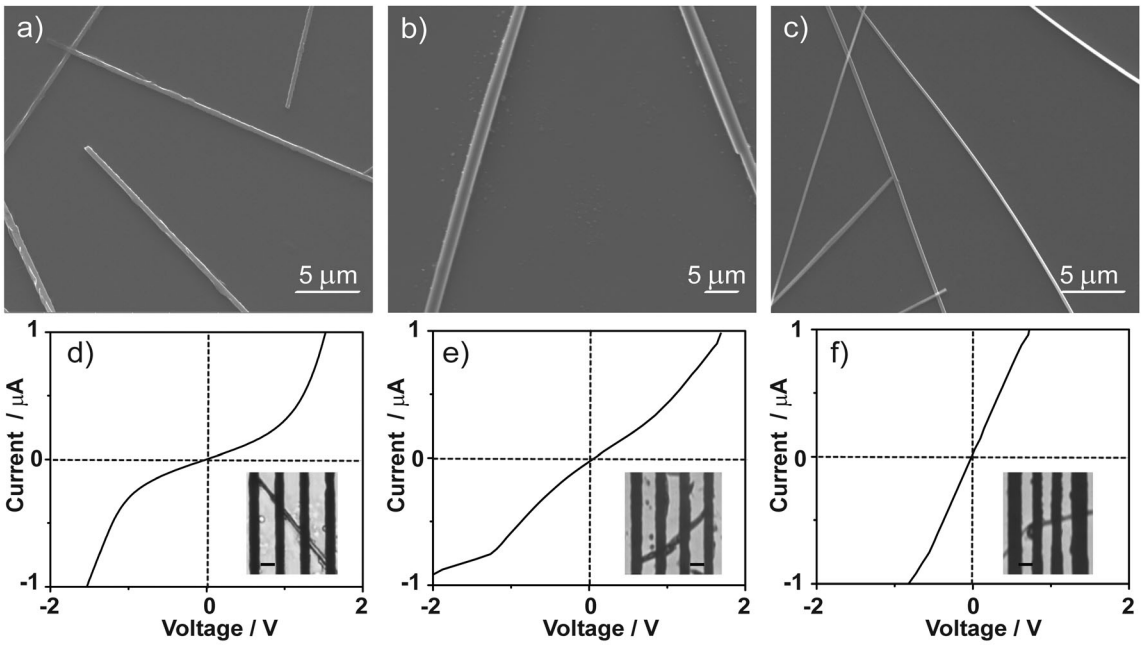

Fig. 4 SEM images of the wire structures (a) Au-BEDT-TTF (**23**) (diameter, 0.56 ± 0.12 μm), (b) Cu-BEDT-TTF (**25**) (diameter, 2.11 ± 0.53 μm) and (c) Fe-BEDT-TTF (**27**) (average diameter, 0.47 ± 0.11 μm) generated on the four-inlet microchip. (d–f) *I–V* curves of single wires from **23**, **25** and **27**, respectively. Figure insets in (d–f) show the aligned single nano-/microwire on the microelectrodes.

and quantitatively. Thus, these results clearly show that the C_1 substitution of the aldehyde group on the TTF units (Fig. S2, ESI†) didn't block the stacking of the TTF units, meanwhile, the active side groups could be preserved in the charge transfer complexes.

To better understand the role of substitute groups in TTF derivatives, other TTF-based compounds that have additional sulphur atoms at the periphery of the TTF skeleton were chosen,[32] such as TET-TTF, TCE-TTF and BEDT-TTF. In one case, TET-TTF and TCE-TTF, which have short alkyl groups connected to sulphur at the C_1, C_2-position (Fig. S2, ESI†), didn't result in obvious wire structures after reacting with $HAuCl_4$ and $CuCl_2$ (Fig. S19, ESI†), which might be due to the low stacking capabilities of these molecules.[17] In another case, BEDT-TTF, which has sulphur-containing planar ring frames substituted at the C_1, C_2-position of TTF (Fig. S2, ESI†),[33] was used to react with $HAuCl_4$, Cu(II) and Fe(III) salts. Here, a two-solvent system was applied, with metal salts dissolved in CH_3OH (0.06 mM) and BEDT-TTF in THF (0.24 mM), owing to its low solubility in CH_3CN. As indicated in Fig. S20 (ESI†), the absorbance spectra proved the charge transfer between the metal ions and BEDT-TTF. Although M-BEDT-TTF showed rods or large wire-like structures in bulk (Fig. S21, ESI†), all the structures obtained from microchips exhibited nano-/microwire morphologies (Fig. 4 and Fig. S22, ESI†). Au-BEDT-TTF (**23**) and Fe-BEDT-TTF (**27**) formed nanowires (Fig. 4a and c), while Cu-BEDT-TTF (**25**) resulted in microwires (Fig. 4b). The comparison between the morphologies of the structures from M-TET-TTF, M-TCE-TTF and M-BEDT-TTF indicated that for the C_1, C_2-position substituted TTF derivatives with sulphur, the planar ring structure was more favourable than a short alkyl group for a strong molecular interaction to form stacking structures.[17,34]

BEDT is known as an excellent electron donor to form various charge transfer compounds that show a wide range of electrical conductivities from insulators or semiconductors to organic metals, according to the different compositions.[35] Thus, the conductivities of single M-BEDT-TTF nano-/microwires were also measured by aligning single wires on microelectrodes, as for other M-TTF-based nanostructures. As shown in Fig. 4, all structures derived from the BEDT-TTF-based complexes (**23**, **25** and **27**) exhibited non-linear *I–V* curves with a current sweeping range of −1 μA to +1 μA, indicating the conductive properties of these wires at room temperature. However, an attempt to acquire the *I–V* curves of structures from **24** and **26** was not successful in our experiment (Fig. S22b and d, respectively, ESI†). For compounds **23**, **25** and **27**, the electrical conductivities of M-BEDT-TTF nano-/microwires were calculated from the linear part of the *I–V* curves in Fig. 4, which were 6.3×10^{-3} S cm^{-1}, 4.8×10^{-3} S cm^{-1} and 1.2×10^{-2} S cm^{-1}, respectively (Fig. S23, ESI†). These obtained conductivity values are comparable to the reported values of other Cu-BEDTTTF powder products.[20,36] Due to the low product yield of M-BEDT-TTF complexes, IR and EA were not performed. However, the EDX-SEM spectra were obtained to confirm the composition of **23**, **25** and **27**. As indicated in Fig. S24 (ESI†), it is noticeable that C and S elements increased obviously in these M-BEDT-TTF wires, compared to the spectrum of glass slide. In addition, Cu and Fe elementals were confirmed from the spectrum of **25** and **27** separately.

4 Conclusions

In summary, we presented a comprehensive overview on different metal and TTF-based compounds (Table 1) and showed the

influence of the different preparative conditions, including bulk (non-flow) *vs.* laminar flow conditions, on the morphology. The results proved that a four-inlet microchip with laminar flow and solvent sheath streams was an efficient technique to obtain long and thin nanowires. At this point it should be noted that the concentration ratio of the precursors also influences the morphology of the assembled structures. Variations of the feed molar ratio may result in the formation of particles instead of wires as shown for Au-TTF.[19] This and other parameters affecting the morphology can be studied in the microfluidic devices in the future.

With the help of single wire conductivity measurement, we successfully sorted out the single nanowires with good conductivity behaviours at room temperature, which could be used for building nanodevices. The comparison between M-TTF and M-TTF derivatives indicated that M-TTF, M-FTTF and M-BEDT-TTF can result in wire structures, while M-TET-TTF and M-TCE-TTF can only form crystals. Thus, for the C_1, C_2-position substituted TTF derivatives with sulphur, the planar ring structure can form stacking structures, much easier than those with short alkyl groups under the reaction conditions in our work. Among the M-TTF (and derivatives) systems we studied, the nanowires derived from M-TTF and M-FTTF exhibited high electrical conductivities from 10^{-1} to 10^{1} S cm^{-1} at room temperature, which are one or two orders higher than those for M-BEDT-TTF, in accordance with previously reported work. The resulting overview table is a means to select structures with desired properties, *e.g.* for sensing applications with a high conductivity. In the future, the sensing abilities of different TTF-based wire structures for various analytes, particularly volatile organic compounds, will be studied and compared.

Acknowledgements

We thank the Scientific Center for Optical and Electron Microscopy (ScopeM) of ETH Zurich for their facilities. We also want to thank Dr Daniel Schaffhauser for the great help with the conductivity measurement and valuable discussion on the results, Yannick Schmid for the fabrication of glass slides with microelectrodes, and Dr Princia Salvatore of ISAS Berlin for the very useful discussion on the conductivity results. Funding from the Excellence Initiative of the German Research Foundation (DFG) and the Ministerium für Innovation, Wissenschaft und Forschung des Landes Nordrhein-Westfalen, the Senatsverwaltung für Wirtschaft, Technologie und Forschung des Landes Berlin, and the German Bundesministerium für Bildung und Forschung are gratefully acknowledged.

References

1 M. A. Bangar, D. J. Shirale, W. Chen, N. V. Myung and A. Mulchandani, *Anal. Chem.*, 2009, **81**, 2168–2175.
2 K. S. Park, B. Cho, J. Baek, J. K. Hwang, H. Lee and M. M. Sung, *Adv. Funct. Mater.*, 2013, **23**, 4776–4784.
3 A. Pescaglini and D. Iacopino, *J. Mater. Chem. C*, 2015, **3**, 11785–11800.
4 N. T. Kemp, D. McGrouther, J. W. Cochrane and R. Newbury, *Adv. Mater.*, 2007, **19**, 2634–2638.
5 I. Imaz, M. Rubio-Martínez, W. J. Saletra, D. B. Amabilino and D. Maspoch, *J. Am. Chem. Soc.*, 2009, **131**, 18222–18223.
6 J. Puigmartí-Luis, M. Rubio-Martínez, U. Hartfelder, I. Imaz, D. Maspoch and P. S. Dittrich, *J. Am. Chem. Soc.*, 2011, **133**, 4216–4219.
7 X. Chen, A. Kis, A. Zettl and C. R. Bertozzi, *Proc. Natl. Acad. Sci. U. S. A.*, 2007, **104**, 8218–8222.
8 V. Coropceanu, J. Cornil, D. A. da Silva Filho, Y. Olivier, R. Silbey and J.-L. Brédas, *Chem. Rev.*, 2007, **107**, 926–952.
9 Y. Xia, P. Yang, Y. Sun, Y. Wu, B. Mayers, B. Gates, Y. Yin, F. Kim and H. Yan, *Adv. Mater.*, 2003, **15**, 353–389.
10 A. C. Grimsdale and K. Müllen, *Angew. Chem., Int. Ed.*, 2005, **44**, 5592–5629.
11 M. R. Bryce, *Adv. Mater.*, 1999, **11**, 11–23.
12 W. Suzuki, E. Fujiwara, A. Kobayashi, Y. Fujishiro, E. Nishibori, M. Takata, M. Sakata, H. Fujiwara and H. Kobayashi, *J. Am. Chem. Soc.*, 2003, **125**, 1486–1487.
13 J. L. Segura and N. Martín, *Angew. Chem., Int. Ed.*, 2001, **40**, 1372–1409.
14 Y. I. Kim and W. E. Hatfield, *Inorg. Chim. Acta*, 1991, **188**, 15–24.
15 M. B. Inoue, M. Inoue, Q. Fernando and K. W. Nebesny, *Inorg. Chem.*, 1986, **25**, 3976–3980.
16 S.-N. Choi, W.-S. Jung, M.-J. Lee, Y.-M. Lee and Y.-I. Kim, *Polyhedron*, 2004, **23**, 2111–2115.
17 K. Naka, D. Ando and Y. Chujo, *Synth. Met.*, 2009, **159**, 931–934.
18 Y. Geng, X.-J. Wang, B. Chen, H. Xue, Y.-P. Zhao, S. Lee, C.-H. Tung and L.-Z. Wu, *Chem. – Eur. J.*, 2009, **15**, 5124–5129.
19 K. Naka, D. Ando, X. Wang and Y. Chujo, *Langmuir*, 2007, **23**, 3450–3454.
20 R. Kanehama, M. Umemiya, F. Iwahori, H. Miyasaka, K.-i. Sugiura, M. Yamashita, Y. Yokochi, H. Ito, S.-i. Kuroda, H. Kishida and H. Okamoto, *Inorg. Chem.*, 2003, **42**, 7173–7181.
21 B. Z. Cvetković, J. Puigmartí-Luis, D. Schaffhauser, T. Ryll, S. Schmid and P. S. Dittrich, *ACS Nano*, 2013, **7**, 183–190.
22 Y. Xing, A. Wyss, N. Esser and P. S. Dittrich, *Analyst*, 2015, **140**, 7896–7901.
23 A. L. Thangawng, P. B. Howell Jr, J. J. Richards, J. S. Erickson and F. S. Ligler, *Lab Chip*, 2009, **9**, 3126–3130.
24 J. Puigmarti-Luis, D. Schaffhauser, B. R. Burg and P. S. Dittrich, *Adv. Mater.*, 2010, **22**, 2255–2259.
25 Y. Xia and G. M. Whitesides, *Annu. Rev. Mater. Sci.*, 1998, **28**, 153–184.
26 X. Q. Wang, H. Itoh, K. Naka and Y. Chujo, *Langmuir*, 2003, **19**, 6242–6246.
27 A. R. Siedle, G. A. Candela, T. F. Finnegan, R. P. Vanduyne, T. Cape, G. F. Kokoszka, P. M. Woyciejes and J. A. Hashmall, *Inorg. Chem.*, 1981, **20**, 2635–2640.
28 B. J. Hathaway, D. G. Holah and J. D. Postlethwaite, *J. Chem. Soc.*, 1961, 3215–3218.

29 R. Bozio, I. Zanon, A. Girlando and C. Pecile, *J. Chem. Phys.*, 1979, **71**, 2282–2293.
30 N. F. Curtis and Y. M. Curtis, *Inorg. Chem.*, 1965, **4**, 804–809.
31 J. Puigmarti-Luis, J. Stadler, D. Schaffhauser, A. P. del Pino, B. R. Burg and P. S. Dittrich, *Nanoscale*, 2011, **3**, 937–940.
32 T. Jorgensen, T. K. Hansen and J. Becher, *Chem. Soc. Rev.*, 1994, **23**, 41–51.
33 M. Mas-Torrent, P. Hadley, S. T. Bromley, X. Ribas, J. Tarrés, M. Mas, E. Molins, J. Veciana and C. Rovira, *J. Am. Chem. Soc.*, 2004, **126**, 8546–8553.
34 J. J. Novoa, M. C. Rovira, C. Rovira, J. Veciana and J. Tarrés, *Adv. Mater.*, 1995, **7**, 233–237.
35 H. H. W. J. M. Williams, T. J. Emge, U. Geiser, M. A. Beno, P. C. W. Leung, K. D. Corlson, R. J. Thorn, A. J. Schultg and M.-H. Wangbo, *Progress in Inorganic Chemistry*, Wiley, New York, 1987.
36 U. Geiser, H. H. Wang, C. E. Hammond, M. A. Firestone, M. A. Beno, K. D. Carlson, L. Nunez and J. M. Williams, *Acta Crystallogr., Sect. C: Cryst. Struct. Commun.*, 1987, **43**, 656–659.